Self-wrinkling induced by Darrieus-Landau instability in turbulent premixed Bunsen flames from low to moderately high Reynolds numbers

G. Troiani [1,*] P. E. Lapenna [2] R. Lamioni [3] and F. Creta [2]
[1]ENEA C.R. Casaccia, 00123 Rome, Italy
[2]Dept. of Mechanical and Aerospace Engineering, Sapienza University of Rome, 00184 Rome, Italy
[3]Dept. of Civil and Industrial Engineering, University of Pisa, 56126 Pisa, Italy

(Received 23 November 2021; accepted 28 April 2022; published 20 May 2022)

Experimental data obtained via particle image velocimetry are used to investigate the self-wrinkling of premixed flame fronts induced by Darrieus-Landau (DL) instability and its interaction with turbulence from low to moderately high Reynolds numbers in a Bunsen configuration. At low Reynolds, hence in quasilaminar conditions, the DL instability is experimentally triggered by varying the mixture ratio. Conversely, in turbulent cases, the DL instability is triggered by varying the Bunsen nozzle diameter so that flames can be compared at the same equivalence ratio and jet Reynolds numbers. The differences between stable and unstable Bunsen flames at low Reynolds number are discussed in terms of vorticity generation downstream in the flame as well as total flame strain and its normal and tangential components. The straining pattern of a single DL cusp is calculated along the flame front to create a reference case for higher turbulence intensity cases and assess the influence of self-wrinkling of the flame front on the reactant flow field, i.e., the channeling effect. The results obtained are consistent with recent direct numerical simulations of single DL-cusp propagating in a quiescent environment. In addition, inspection of strain-curvature joint probability density function, curvature correlation coefficient and crossing length statistics will show that, even from the intermediate Reynolds numbers explored, unstable flames under the influence of self-wrinkling effects possess the statistical characteristics that stable flames gain only at high turbulence levels, where a unified and turbulence dominated regime is likely to be reached, although with the persistence of some residual differences.

DOI: 10.1103/PhysRevFluids.7.053202

I. INTRODUCTION

More than two decades ago, Clanet and Searby carried out the first experimental study of the Darrieus-Landau (DL) intrinsic instability measuring its growth rate in a planar laminar premixed flame front [1]. Since then, it has become apparent that, in a laminar scenario, such intrinsic instabilities have a significant role in determining the morphological and propagative characteristics of a premixed flame [2–4], as confirmed by many dedicated experiments [5,6] and direct numerical simulations (DNSs) [7,8]. Hydrodynamic or Darrieus-Landau intrinsic instabilities are clearly manifested in the form of large-scale cusp-like corrugations or self-wrinkles of the flame front, where the instability mechanism is driven by thermal expansion [9,10]. At sufficiently small scales, the DL mechanism is balanced by the stabilizing mechanism of diffusive nature [11–13] when the Lewis number of the fuel is larger than the critical value [14], which is the only case discussed in the present work.

*guido.troiani@enea.it

The interplay between DL instability-induced self-wrinkling and turbulence is an active research topic which has largely benefited from the availability of numerical simulations. From a physical perspective, significant contributions have been made employing numerical techniques ranging from weakly nonlinear models [15,16] to hybrid approaches such as the Navier-Stokes and front-capturing methodology [17–19] stemming from the hydrodynamic theory of flames [13]. More recently, DNS dedicated to the investigation of DL instability and its interaction with turbulence have been developed in both two-dimensional [20–23] and three-dimensional settings [24], providing reliable data sets. In addition, simulations dedicated only to flames self-wrinkling [8,25], are also of interest from the modeling perspective [26], since the role of DL instability in turbulent combustion modeling of premixed flames is still not completely understood. However, both the geometrical scale [24] and the Reynolds number Re of DNS dedicated to DL instability is inherently limited by their computational cost. In this context, experiments remain a fundamental tool to understand the phenomena at play when Re approaches moderate to high values, hence when turbulence is expected to mitigate the DL effect, as discussed in the review paper by Lipatnikov and Chomiak [27] and in many relevant studies based on various approaches such as renormalization analysis [28–30], spectral formulations [31,32], and the perturbed Sivashinsky equation [16].

Experimental investigations focusing on the interaction between turbulence and the DL-instability have been mainly performed using Bunsen and spherical expanding flame configurations. The latter configuration has been used by Yang *et al.* [33] to investigate the role of the DL instability in the propagation of expanding flames in a turbulent environment using high pressure to promote the onset of instability. In particular, following the pioneering work of Boughanem and Trouvè [34], Yang *et al.* [33] compared the characteristic timescales of the DL instability and turbulence, and they identified two extreme regimes called, respectively, *instability dominated* and *turbulence dominated*. On the other hand, the DL-instability has been observed also in Bunsen as well as slot burners, where the interaction with the flow is further complicated by the presence of shear-generated fluctuations and turbulence.

Schlimpert *et al.* [35] studied the interaction between the DL-instability and shear layers in turbulent premixed combustion using a slot flame configuration in order to extract a flame transfer function. Using a Bunsen burner configuration, Troiani *et al.* [36] showed the existence of two distinct scaling laws for the turbulent flame speed of propane-air mixtures depending on the presence or absence of the DL instability, triggered by varying the equivalence ratio. Creta *et al.* [20] have demonstrated that the DL instability can be effectively investigated by comparing DL-unstable and DL-stable flames at the same Re, where the DL onset is triggered by an increasing Bunsen diameter. The effect of the density ratio in promoting the DL-instability onset and its influence on the turbulent flame speed was also investigated experimentally by Lipatnikov *et al.* [37]. More recently, Wang *et al.* [38] investigated the effect of the burner dimension on the structure of turbulent premixed flames, eventually influenced by the DL instability at large burner diameters. More recently, Wang *et al.* [39] employed methane mixtures in Bunsen burners of various dimensions at Re between 1000 and 8500, aiming at the quantification of DL effects and introducing the concept of proportion of effective disturbances. Experimental results at higher Re have been discussed by Lapenna *et al.* [40] in terms of flame morphology and propagation speed up to $Re = 10000$, using DNS data to support such observations. Also observed was the persistence of residual differences between DL-stable and DL-unstable flames, despite the standard index of the DL-instability, namely, the skewness of the curvature probability density function (p.d.f.) [20] indicated the attainment of a unified, turbulence-dominated regime. This aspect is an additional motivation for the present work, which is dedicated to the investigation of the residual DL effects at moderately high Re [41]. In addition, we address the characterization of DL effects on low-Re Bunsen flames, using experimental data to shed light on the straining patterns and flame vorticity production, previously investigated in laminar and weakly turbulent setting by means of DNS [21] and in a more practical configuration by Steimberg *et al.* [42,43]. Toward this purpose, it should be stressed that, near the burner rim, where flow velocities are generally lower than the bulk velocity, hydrodynamic disturbances can

develop and eventually get convected downstream before their complete growth. By means of linear stability analysis [44] the maximum growth rate for a disturbance of the extent of the most unstable wavelength in the Darrieus-Landau instability can be evaluated and compared with the timescale associated with a Bunsen flame characterized by a bulk velocity and a mean flame height. When such timescales are of the same order of magnitude, which is generally the case of slot or Bunsen flames found in literature, it can be concluded that hydrodynamic DL disturbances have the time to develop because they are convected downstream and that their eventual depletion has to be considered an effect of the interplay with turbulent velocity fluctuations of the flow field.

In this framework, the objective of the present work is to glean insight from well-established experimental data sets [20,22,40] to (i) obtain a complete characterization of low-*Re* Bunsen flames in the presence of a DL instability; (ii) investigate the interplay of a DL instability and turbulence in terms of flame front fluctuations using crossing length concepts, strain-curvature joint p.d.f. and curvature correlation coefficient. Using these results, the role of DL-induced self-wrinkling effects can be discussed, showing that DL-unstable flames promote statistical characteristics that stable flames will exhibit only at high turbulence levels [45]. Our data confirm that, at high *Re*, a unified and turbulence-dominated regime is likely to be reached, although with the persistence of some residual morphological differences between DL-stable and DL-unstable flames.

II. METHODS

To investigate and discuss the self-wrinkling and flame strain induced by DL instability at different Reynolds numbers, we employ a well-established experimental data set [20] that was recently extended to $Re = 10\,000$ [40]. This data set was obtained by using Bunsen burner configurations at atmospheric pressure fed with a mixture of air and propane at variable equivalence ratio ϕ. Two Bunsen diameters D are employed in order to obtain (i) a set of DL-stable, small-scale flames with $D = 9$ mm; (ii) a set of DL-unstable, large-scale flames with $D = 18$ mm. As discussed by Lapenna *et al.* [24], turbulent premixed flames are conventionally denoted as large scale, or, equivalently, DL unstable when the reference hydrodynamic length scale L is larger than the cutoff length λ_c, determined either by linear stability analysis via dedicated DNS [46] or via hydrodynamic theory [14]. For a Bunsen flame configuration, the diameter D is usually taken as the reference hydrodynamic length scale L. The two diameters were thus selected such that $9\text{ mm} < \lambda_c < 18\text{ mm}$ over the entire range of ϕ employed [20]. In fact, for these two diameters, no significant effect was noticed on the flame morphology varying the equivalence ratio [40], so we are using only $\phi = 1.4$ from that data set for the present investigation. On the other hand, in order to have a reference baseline comparison between a DL-stable and a DL-unstable flame at quasilaminar, low-Reynolds conditions, as numerically done for instance by Lamioni *et al.* [21], we employ an intermediate diameter of $D = 14$ mm. Such an intermediate diameter, for the same propane-air mixture, allows the DL instability to be induced by changing ϕ as done by Troiani *et al.* [36] in the same configuration. The mentioned reference quasilaminar condition, characterized by $Re = 1500$, is obtained with the smallest mass flow rate attainable before flashback occurs. As a result, it can be effectively considered *quasilaminar* and the observable flame wrinkling be directly attributed to DL instability as flow fluctuations are expected to be rather limited. The equivalence ratio of these two flames is purposely selected so as to reproduce a DL-unstable ($\phi = 1.5$) and a DL-stable ($\phi = 0.8$) scenario for such an intermediate Bunsen diameter($D = 14$ mm). A brief summary of all the flames considered in the present experimental investigation is given in Table I. In this table, the effective Lewis number is also reported to assess that thermal diffusive effects have a stabilizing role at the small scales. Operatively, we started from a chemical reaction described by a single overall irreversible step in the form [14,47]

$$\nu_E \mathcal{M}_E + \nu_D \mathcal{M}_D \rightarrow \text{Products}, \tag{1}$$

TABLE I. Summary of the main experimental flow and flame parameters. The Reynolds number is defined by means of the reactants mass flow rate $\dot{m}$, Bunsen diameter D, and the dynamic viscosity of reactants μ as $Re = 4\dot{m}/\pi\mu D$.

Bunsen diameter	Reynolds number	Equivalence ratio	Effective Lewis
$D = 14$ mm	$Re = 1500$ (quasilaminar)	$\phi = 0.8, 1.5$	$Le_{\text{eff}} = 1.76, 1.36$
$D = 9$ mm	$Re = 2500, 5000, 7000, 10000$	$\phi = 1.4$	$Le_{\text{eff}} = 1.38$
$D = 18$ mm	$Re = 2500, 5000, 7000, 10000$	$\phi = 1.4$	$Le_{\text{eff}} = 1.38$

where $\mathcal{M}_{E,D}$ represents the excess and deficient reactants and ν is taken of order unity, the effective Lewis number of the mixture is then given as

$$Le_{\text{eff}} = 1 + \frac{(Le_E - 1) + (Le_D - 1)A}{1 + A}, \tag{2}$$

with $A = 1 + \beta(\Phi - 1)$, β being the Zeldovich number, and $\Phi = \phi$ the equivalence ratio, when the mixture is rich ($\phi > 1$) and $\Phi = \phi^{-1}$ for lean mixtures. Deficient and excess reactants can be either the fuel under investigation or the oxygen, depending on the amount of air used, i.e., a lean or rich mixture.

The experimental setup employs a diffusive pilot flame to prevent potential flame blow-off at moderate to high Reynolds numbers [48]. A particle image velocimetry (PIV) system probes the velocity field on a plane scanned by a 0.4-mm-thick laser sheet generated by a cylindrical lens. Alumina particles with a characteristic dimension of 3 μm are dispersed into the flow and they guarantee unbiased probing of flow velocity across the flame front [49,50]. The flame front position is determined from the sudden variation of the particle number density caused by the reacting layer in premixed flames [51,52]. This corresponds to zones of very different levels of light intensity within the Mie scattering images. For all the flames investigated, turbulent combustion occurs in the flamelet regime as educed by inspection of Table II, where the main parameters of the flames realized are reported, and the Borghi-Peters diagram of Fig. 1 with the experimental flames reported. Therefore, a nearly bimodal intensity distribution is expected, clearly distinguishing unburnt from burnt density. Operationally, from any single binarized image of the instantaneous flame front, the flame contour is extracted by setting a threshold intensity level. A signed distance function ψ

TABLE II. The main turbulence characteristics of the experimental flames are analyzed. The columns give the turbulent fluctuations u_0', the autocorrelation length scale ℓ, the unstrained laminar combustion velocity S_L^0 at equivalence ratio $\phi = 1.4$, and the corresponding thermal thickness δ_T based on the maximum temperature gradient. Having the flame at $Re = 2500$ gives a very low level of fluctuations, so it is considered quasilaminar and the correlation coefficient is not indicated. Laminar flame characteristics are evaluated by means of GRI-Mech 3.0 mechanism [53]. Velocities are in ms^{-1} and lengths in millimeters.

	Reynolds number	u_0'	ℓ	S_L^0	δ_T
	2500	0.2		0.28	0.5
$D = 18$ mm	5000	0.6	0.96	0.28	0.5
	7000	1.0	0.65	0.28	0.5
	10 000	1.4	0.53	0.28	0.5
	2500	0.1		0.28	0.5
$D = 9$ mm	5000	0.5	0.6	0.28	0.5
	7000	1.1	0.4	0.28	0.5
	10 000	1.8	0.3	0.28	0.5

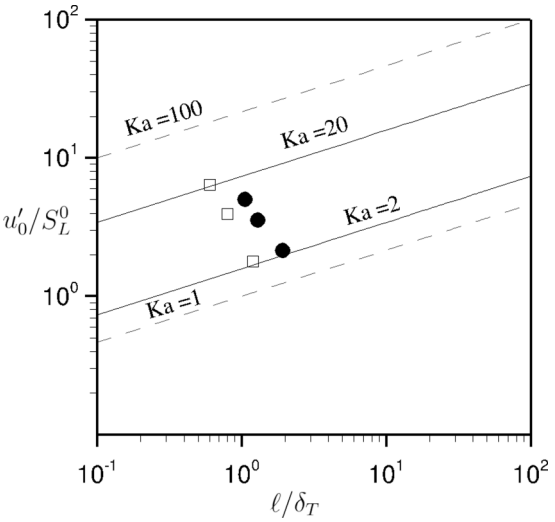

FIG. 1. Borghi-Peters diagram. Open symbols, $D = 9$ mm, filled symbols, $D = 18$ mm. Constant Karlovitz scaling laws follow from $u'_0/S^0_L = Ka^{2/3}\ (\ell/\delta_T)^{1/3}$.

is evaluated with positive and negative values indicating products and reactants, respectively. As a result, the normal to the flame is constructed towards the products as $\mathbf{n} = \nabla\psi/|\nabla\psi|$ and the flame curvature is expressed as $\kappa = -\nabla \cdot \mathbf{n}$. As discussed by Lamioni *et al.* [22], in order to evaluate the flame straining patterns using the PIV data, the tangential strain [14] a_T is deprived of the divergence of the velocity field $\nabla \cdot \mathbf{u}$ to obtain the flame strain $K_S = a_T - \nabla \cdot \mathbf{u}$. In addition, decomposing the velocity field at the reacting front into normal and tangential components as $\mathbf{u} = u_n\mathbf{n} + \mathbf{u}_\tau$, the flame strain can be decomposed into two components [14,44], $K_S = K_S^n + K_S^\tau$ with $K_S^n = -u_n\kappa$ being the normal and $K_S^\tau = \nabla_\tau \cdot \mathbf{u}_\tau$ being the tangential component.

III. RESULTS

A. Reference low-*Re* flame characterization

The typical DL-induced features on laminar premixed flames, usually investigated in a planar setting [6], are discussed here in the context of a Bunsen flame configuration. The two low-*Re* flames at $Re = 1500$ are shown in Fig. 2, where significant differences can be observed between the two ϕ cases. In the DL-unstable case ($D = 14$ mm, $\phi = 1.5$), cusp-like structures arise on the flame front, while being convected downstream by the component of the mean flow tangential to the front, as discussed in detail by Ref. [54]. Conversely, such features are clearly absent for the DL-stable case ($D = 14$ mm, $\phi = 0.8$). Note that, as discussed in Ref. [20], the elevated height of the stable flame, resulting from a global consumption speed which is smaller than S^0_L, can be tentatively explained by the presence of buoyancy-induced effects on the flames. Figure 2 also shows the ensemble-averaged progress variable isolines $\overline{c} = 0.1, 0.5, 0.8$. Local DL-induced effects along the flame front of the low-*Re* Bunsen flames are analyzed in terms of velocity field and total flame strain and its components. According to recent findings in the literature [5,17,18] the flow field as seen from an advancing flame front can be considered as a hallmark of hydrodynamic instability. The purpose of this section is to seek a similar flow pattern in Bunsen flames in quasilaminar conditions. A change of the frame of reference is needed to this end, to switch from the actual laboratory frame of reference to another one which is moving with the flame front. Actually, front displacement cannot be obtained by present measurements and the tentative approach followed was to subtract a purposely chosen velocity field to the instantaneous one. Figure 3 shows the flame

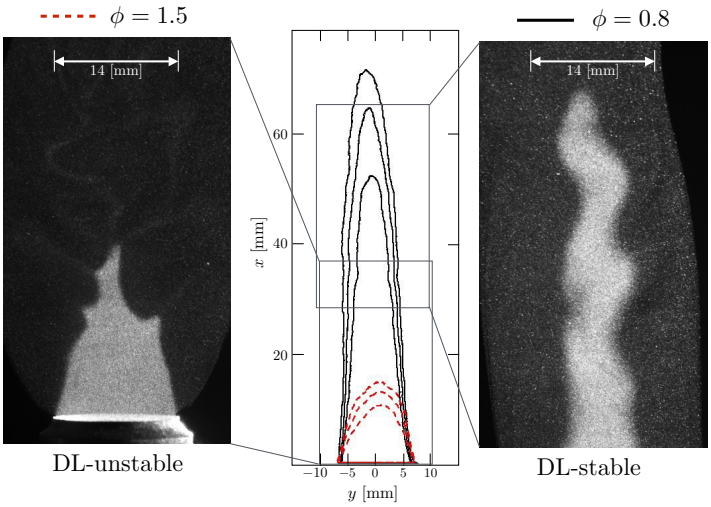

FIG. 2. Low-*Re* Bunsen flames $D = 14$ mm: Mie scattering images of the two cases and mean progress variable $\overline{c}$. Isolines represent progress variables values of $\overline{c} = 0.1, 0.5, 0.8$ for both cases.

strain K_S along the flame front superimposed on a velocity vector field, which is obtained from the instantaneous one by subtracting locally half the ensemble-averaged velocity in order to partially mitigate the convection of the Bunsen flow. In the same figure, the velocity streamlines, mimicking those seen from the evolving flame front, are also shown for the DL-unstable flame with the results of streamlines converging toward cusp apexes. In particular, the streamline-focusing effect can be further refined and highlighted by observing the single cusp labeled with number 1 in the left panel of Fig. 3 for which the radial instantaneous velocity field is added to the unstretched laminar flame speed S_L^0 and a constant value subtracted to the axial velocity field. This constant value is selected to be half the spatially averaged velocity field upstream of the cusp. This procedure can therefore be assimilated to a change of reference from a laboratory frame to a frame moving with the cusp, which is moving towards the Bunsen axis at a velocity comparable to S_L^0, while being convected downstream by half the Bunsen axial velocity. The ensuing result, shown in Fig. 4, is very similar to that observed both numerically and experimentally in laminar DL-unstable flames propagating in a quiescent environment [6,21].

Before analyzing the strain rate K_S it is worth stressing that values of K_S analyzed are evaluated by means of the instantaneous velocity field in the frame of reference of the laboratory. This is because the subtraction of a spatially evolving flow field would change the velocity gradients at the flame front involved in the evaluation of flame strain. On the other hand, the flame-strain evaluation is invariant to any transformation when the subtracted velocity field is constant in space, as in the case reported in Figs. 4 and 5(a). In the DL-unstable case of Fig. 3, K_S assumes largely positive values at the cusp apex, where the curvature is highly negative. On the other hand, K_S is characterized by negative values at the cusp sides. In the DL-stable case, on the other hand, a less extended range of strain and curvature values along the flame front are observed.

Along the single cusp previously described, the total strain K_S and its components, along with the flame curvature, have been calculated and reported in Fig. 5(a). The flame front is subjected to a compression given by the tangential strain contribution K_S^τ which originates from the focusing effect of streamlines towards the cusp apex, as highlighted in Fig. 4. Concurrently, the normal strain contribution K_S^n is largely positive, thus making the total strain positive, hence subjecting the flame front to an expansion. Such elevated positive values of the normal component of strain K_S^n can be related to the enhanced normal velocity to which the flame front is subjected in the cusp region, which we denote as a channeling effect. Overall, this combined effect of compression

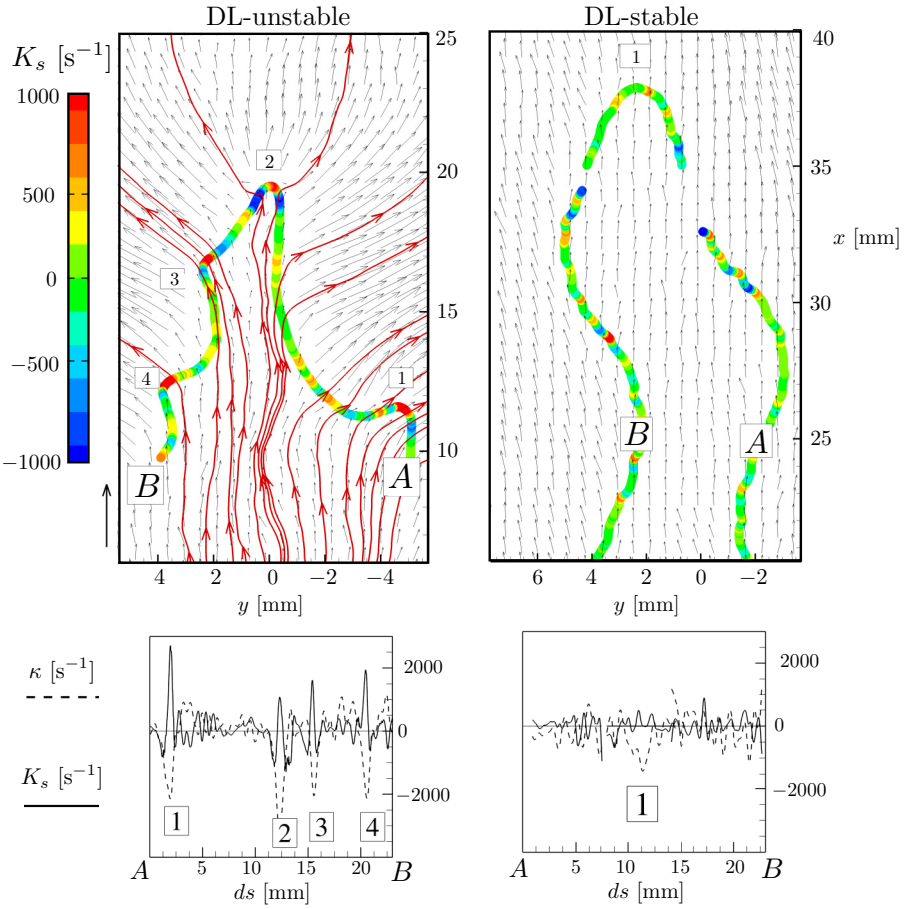

FIG. 3. Vector field visualization of the low-*Re* Bunsen flames obtained from the instantaneous velocity by subtracting half of the two-dimensional ensemble-averaged velocity flow field. Vectors are shown using half of the actual resolution and a reference vector of 5 m/s is also reported. The flame front is colored by the local flame-strain values. For the DL-unstable flame the velocity streamlines are shown. Flame strain and curvature are also displayed as functions of the local coordinate ds following the flames from A to B.

and expansion of the flame front close to the cusp apex results in a negative correlation between strain and curvature as displayed in Fig. 5(b). This result is consistent with numerical simulations of DL-unstable, statistically planar flames propagating in a quiescent environment [21] and is one of the hallmarks of DL instability.

The correlation between the strain components and the flame curvature is now statistically investigated for the two low-*Re* flames. Figure 6 shows the joint probability density function (j.p.d.f.) between each strain component and the flame curvature. The marginal p.d.f. of K_S^n and K_S^τ are also reported in the same figure. For both strain components the DL-unstable case features wider and less symmetric p.d.f.s compared with the DL-stable case. In particular, such p.d.f.s are positively skewed for K_S^n and negatively skewed for K_S^τ, respectively. As clearly observable from the j.p.d.f.s, in the DL-unstable case, higher positive values of K_S^n occur when large negative values of the flame curvature are induced by the DL-instability. Note that the peculiar shape of this joint p.d.f. is caused by the definition of K_S^n and is a common feature of bivariate distributions in which one random variable is proportional to the other. Similarly, more negative values of K_S^τ are more probable in correspondence of negative flame curvatures. In fact, for the DL-stable case, the tangential strain

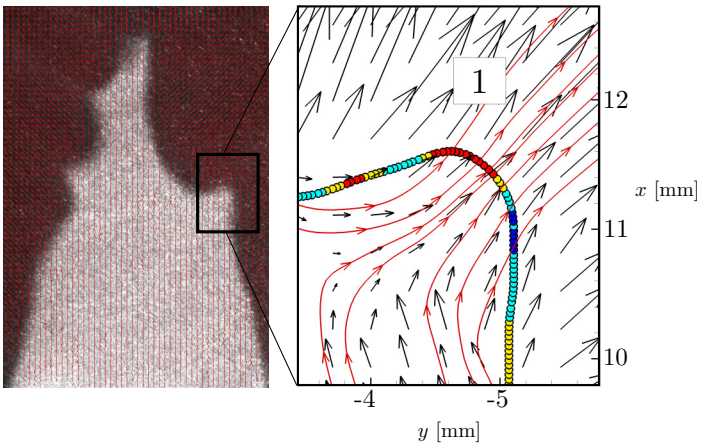

FIG. 4. Detail of the streamline channeling effect induced by a singe DL-cusp as seen from the flame front in the unstable $\phi = 1.5$ case.

and the flame curvature appear to be almost uncorrelated. It is also observable in Fig. 6 that higher absolute values of K_S^n are encountered compared with K_S^τ, which indicates that the results obtained on the single cusp previously analyzed holds, in a statistical sense, over the entire Bunsen flame.

As expected from theory [4] and numerical simulation [17,21], the presence of cusp-like structures induced by the DL-instability has a significant impact not only on the flame but also on the vorticity distribution across and behind the flame front. The DL-instability indeed promotes the baroclinic production of vorticity by amplifying the misalignment between the density and pressure gradients. This scenario is confirmed experimentally in a Bunsen flame setting, as shown in Fig. 7 for the two low-*Re* flames investigated in this section. In fact, the fields of the vorticity ω_z, with z being the direction of the third dimension, show higher absolute values for the DL-unstable case. Figure 7 also displays the vorticity along two distinct streamlines for both flames, highlighting the vorticity production caused by the DL-induced flame morphology.

B. Residual Darrieus-Landau effects at increasing Reynolds number

In this section we employ the second part of the data set, summarized in Table I, namely, the Bunsen flames with $\phi = 1.4$ and $D = 9$ mm (DL-stable) or $D = 18$ mm (DL-unstable) in order to

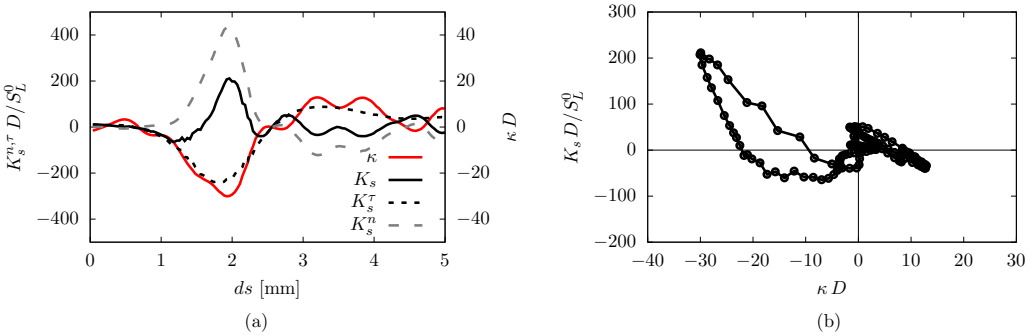

FIG. 5. Flame curvature and strain components along the cusp-like structure marked as [1] in the previous figures. (a) Nondimensional quantities as functions of the flame coordinate $ds = 0 - 5$ mm. (b) Total strain as a function of the flame curvature along the cusp.

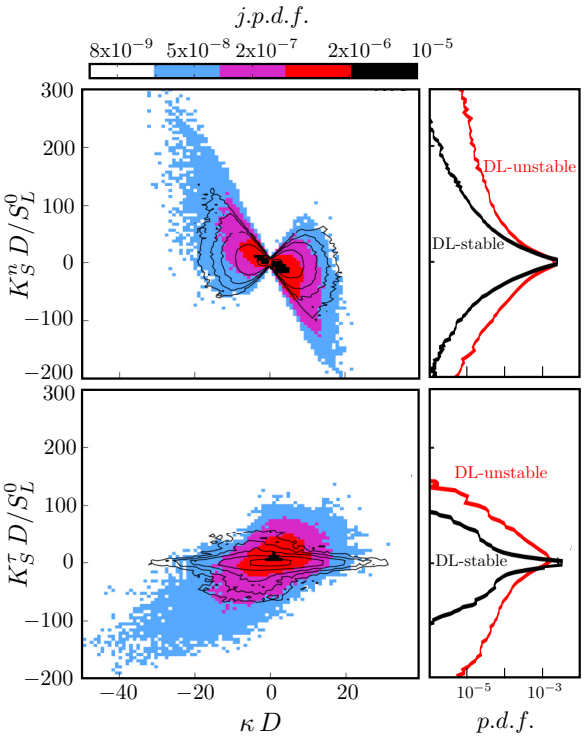

FIG. 6. Joint p.d.f. distribution between the components of flame strain and the flame front curvature k. The colormap refers to the DL-unstable case, while the black isocontour represents the DL-stable case. The marginal distributions of both K_S^n and K_S^τ are also reported.

investigate some of the residual DL effects at increasing Reynolds number. The marked differences between a DL-stable and a DL-unstable case described in the previous section are in fact mitigated as the turbulence intensity increases and a unified turbulence-dominated regime [33] is expected to be reached eventually. As mentioned in the introduction, while well-established DL-instability markers, such as the skewness of flame front curvature p.d.f. [20], may indicate for our data set that a unified regime has been achieved, some relevant differences have been observed to persist [40].

Figure 8 shows both the instantaneous flame fronts and the iso-contour of the mean progress variable for both the DL-unstable cases ($D = 18$ mm) and DL-stable cases ($D = 9$ mm) at increasing Re. As can be observed, as Re increases, more intense velocity fluctuations tend to mitigate the morphological differences between the two sets of flames. A complete description of the flame morphology statistics for these flames has been recently reported [40] and will not be repeated here. This being said, visual differences between the two sets of flames can still be observed at the highest Re available. Quantitatively, the DL enhancement of the turbulent flame speed is clearly reduced as Re increases as reported in Fig. 8. This enhancement is calculated by using the global consumption speed definition [55] and is evaluated by means of the mass flow rate of the mixture through the mean flame area, i.e., $S_T = \dot{m}/(\rho_u A_{\bar{c}=c^*})$ with ρ_u being the unburned mixture density, at a mass flow rate of $\dot{m}$, flowing through the iso-surface A evaluated along the mean flame $\bar{c} = 0.1$ (see Fig. 8). Note that the DL-induced enhancement of the global consumption speed S_T/S_L^0 for the highest Reynolds number case at $Re = 10\,000$ is ≈31.5%, which is a large value if compared with the DL-enhancement calculated by recent DNS simulations, ≈16%, although in a slightly different setting [24]. This confirms the relevant role of residual DL effects at a relatively high Reynolds number of $Re = 10\,000$ and therefore further motivates the following analysis.

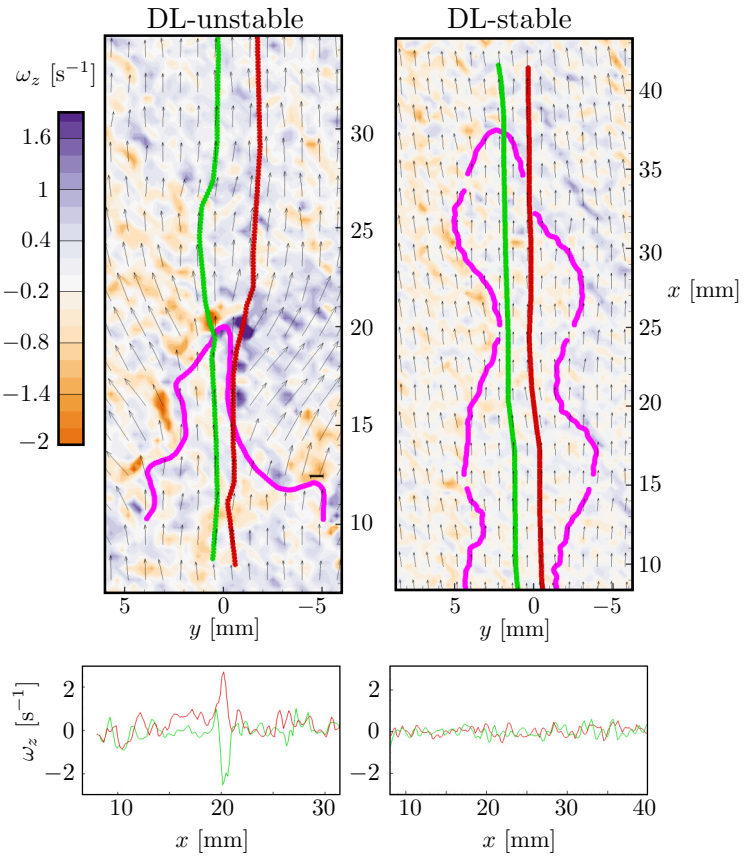

FIG. 7. Instantaneous vorticity fields ω_z in the laboratory frame of reference, with two reference streamlines highlighted for each case. The bottom panels show the vorticity along the reference streamlines using the same color coding.

The effect of the increasing Re on the strain-curvature joint statistics is shown in Fig. 9. At $Re = 2500$, the j.p.d.f. for the DL-unstable case ($D = 18$ mm) is following rather closely the quasilaminar K_S-κ scatter plot taken form Fig. 5(b), with a negative correlation between the strain and the flame curvature. Conversely, the DL-stable cases ($D = 9$ mm) do not exhibit any significant trend, with the j.p.d.f. indicating a rather symmetric marginal distribution for both the variables. As Re is increased toward the highest values of the data set, the bivariate distributions of the DL-unstable case become more symmetric as they diverge from the reference K_S-κ quasilaminar behavior. Conversely, the j.p.d.f.s of the DL-stable case increasingly attain a shape that is qualitatively similar to those corresponding to the DL-unstable flame. Figures 10 and 11 show consequences of the Reynolds number increase on the j.p.d.f.s of the normal and the tangential components of flame strain with curvature, K_S^n-κ and K_S^τ-κ, respectively. In both cases the asymmetric correlation with curvature in the unstable case is found for a Reynolds number up to 5000. At increasing levels of turbulence intensity, velocity fluctuations make the two distributions more symmetric, even though the marginal distribution of curvatures in the upper panels of Fig. 11 remain skewed towards negative curvatures and to a lesser degree as the Reynolds number increases. Conversely, in the stable case, the total flame strain K_S appears to be governed mainly by the normal component of the flame strain K_S^n as its tangential counterpart becomes statistically relevant only at $Re = 10\,000$. However, as some differences remain visible, a completely unified regime does not seem to be achieved, at least for the set of observed flame characteristics.

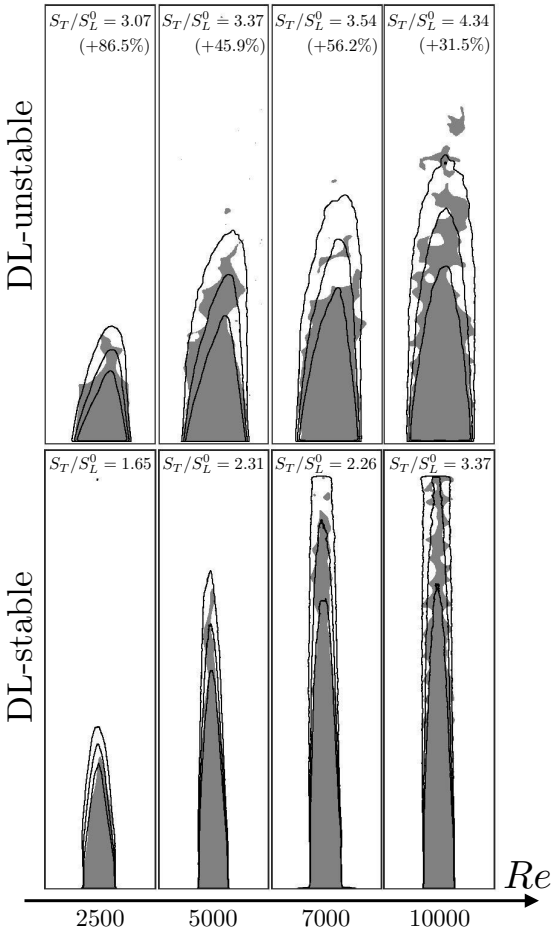

FIG. 8. Binarized images of instantaneous flame fronts for the DL-unstable cases ($D = 18$ mm) and DL-stable cases ($D = 9$ mm) at increasing Re with time-averaged isolines representing $\overline{c} = 0.1, 0.5, 0.9$. The global consumption speed S_T/S_L^0 of each flame is also reported with the relative DL enhancement for the unstable cases.

To better characterize this *resilience to turbulence* [16] of the DL effects at increasing Re, the signal of the curvature κ along the flame front is collected from ≈400 experimental images and the correlation coefficient $C_{\text{corr}}(ds) = \langle \kappa(s)\kappa(s+ds)\rangle / k_{rms}$ calculated along the flame isoline s. The results of this analysis are reported in Fig. 12 for both the Bunsen diameters at increasing Re, displaying C_{corr} as a function of the separation ds along the flame coordinate, normalized with the Bunsen diameter D. The $Re = 2500$ cases have been excluded since their turbulent flow-field is only mildly fluctuating. For the DL-stable cases shown with black lines in Fig. 12 significant differences in C_{corr} profiles can be observed as Re increases. On the other hand, for the DL-unstable cases shown in red in the same figure, an almost Re-independent behavior can be gleaned. The behavior of the C_{corr} profiles can thus be considered to be governed by the DL instability even at low Reynolds numbers, in contrast with the stable cases where the correlation coefficient distribution varies continuously with the Reynolds numbers reaching a shape resembling the Reynolds independence of unstable flames only at $Re = 10\,000$, although maximum values of anticorrelation (minimum value of the correlation coefficient) are reached at different values of ds/D. This result is consistent with a spectral analysis of the flame curvature [40] which has shown that the DL instability is preventing the onset of the -2.4 scaling in power spectral density at intermediate wave numbers [56].

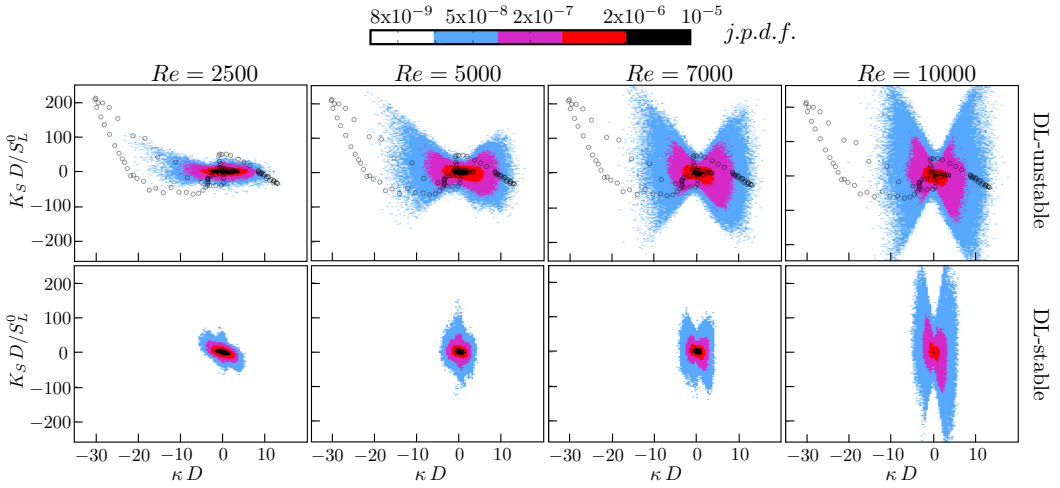

FIG. 9. Joint p.d.f.s between flame strain and curvature for the DL-unstable cases ($D = 18$ mm) and DL-stable cases ($D = 9$ mm) at increasing Re. Superimposed on the DL-unstable cases is K_S vs κ from the quasilaminar single-cusp case shown in Fig. 5(b).

C. Modeling considerations on turbulent scalar fluxes

Residual differences between the two flame series are also of relevance from a modeling standpoint. A set of DNS simulations [24] have shown that DL-unstable flames are characterized by a thicker flame brush, causing a significant reduction of the flame surface density. The same trend has been experimentally confirmed for the flames shown in Fig. 8 by Lamioni *et al.* [22]. This can have a direct impact on the modeling strategies to be adopted in the presence of DL instability, in

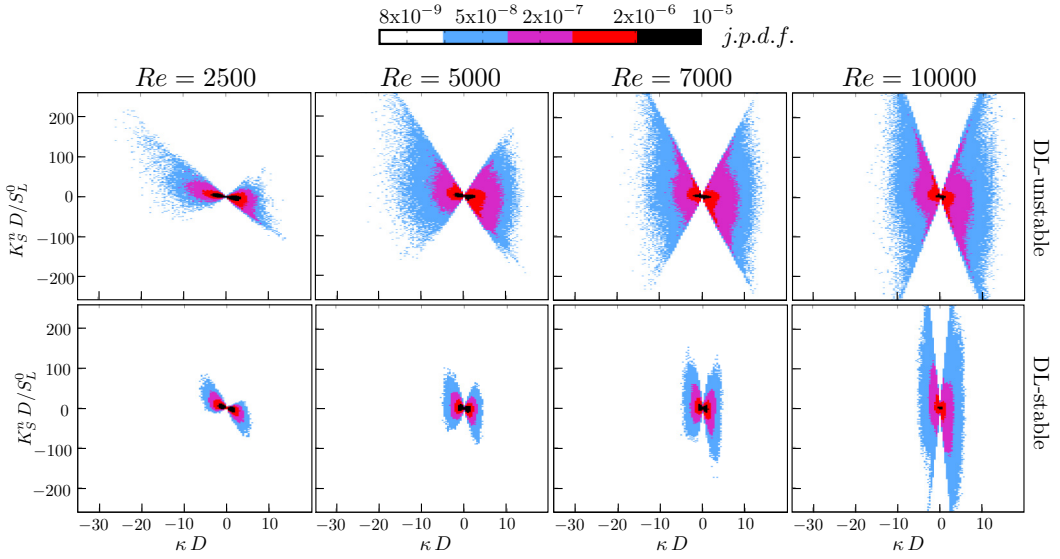

FIG. 10. Joint p.d.f.s between normal component of flame strain K_S^n and curvature for the DL-unstable cases ($D = 18$ mm) and DL-stable cases ($D = 9$ mm) at increasing Re.

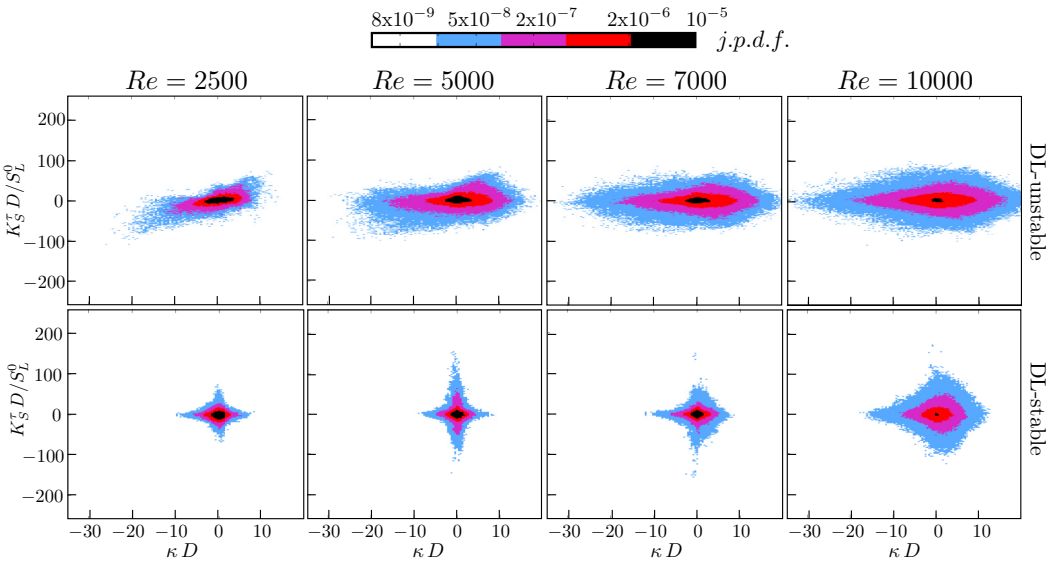

FIG. 11. Joint p.d.f.s between tangential component of flame strain K_S^τ and curvature for the DL-unstable cases ($D = 18$ mm) and DL-stable cases ($D = 9$ mm) at increasing Re.

particular for Reynolds-average Navier-Stokes (RANS) approaches and, to a lesser extent in the large-eddy simulation (LES) context, as recently assessed [26].

In both the RANS and LES contexts, the governing equation for the Favre-averaged and filtered progress variable c reads:

$$\frac{\partial(\bar{\rho}\tilde{c})}{\partial t} + \nabla\cdot(\bar{\rho}\tilde{\mathbf{u}}\tilde{c}) + \nabla\cdot[\bar{\rho}(\widetilde{\mathbf{u}c} - \tilde{\mathbf{u}}\tilde{c})] = \nabla\cdot(\overline{\rho D\nabla c}) + \bar{\omega}, \tag{3}$$

where ρ is the mixture density, $\mathbf{u}$ is the fluid velocity, and ω is the reaction rate of c while $\tilde{\cdot}$ and $\bar{\cdot}$ indicate Favre- and Reynolds-averaged or filtered quantities, respectively. The right-hand side terms of the equation represent the filtered reaction-diffusion which can be modeled by resorting to the

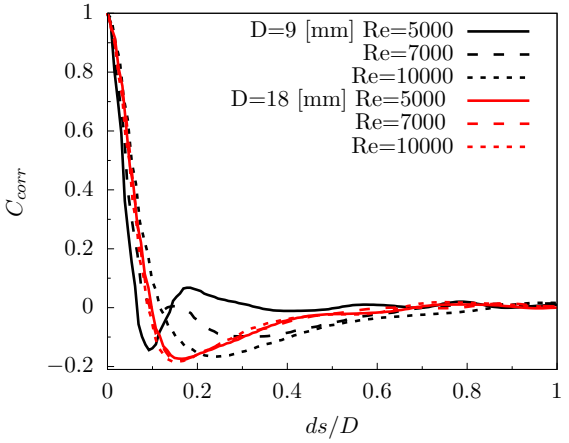

FIG. 12. Correlation coefficient of flame-front curvature as a function of the separation ds along the flame coordinate, normalized by the Bunsen diameter.

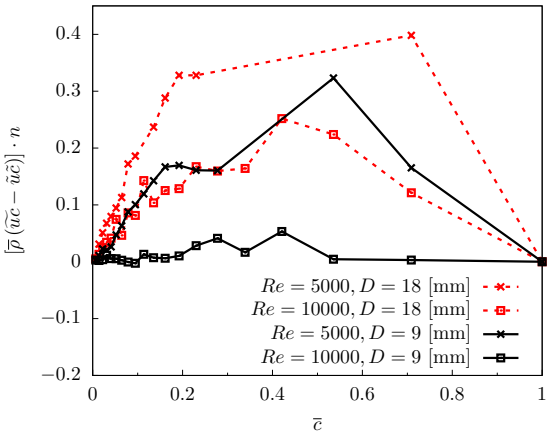

FIG. 13. Turbulent flux of the averaged/filtered progress variable trough the flame brush for DL-stable ($D = 9$ mm) and DL-unstable ($D = 18$ mm) flames.

flame surface density (FSD) concept [57] taking into account intrinsic instability effects [26]. The terms at the left-hand side of the governing equation for averaged and filtered progress variable, correspond respectively to unsteady effects, convective fluxes of the averaged and filtered field, and the unresolved turbulent flux of c. The latter term has been investigated for DL-unstable flames by means of DNS in a two-dimensional setting [21], highlighting that, for a given turbulence intensity, a more pronounced counter-gradient flux is induced by DL effects. Note that counter-gradient-type turbulent diffusion is expected when the flow fluctuations are governed by the flame and its thermal expansion, while standard gradient-type turbulent diffusion is encountered when the flow is governed by turbulent fluctuations [58].

From the experimental standpoint, as discussed by Troiani *et al.* [59], turbulent fluxes can be measured resorting to the Bray-Moss-Libby model (BML) [60] according to which, under the flamelet hypothesis, the turbulent flux depends on the difference between velocities respectively conditioned to combustion products and reactant sides:

$$\overline{\rho}(\widetilde{uc} - \tilde{u}\tilde{c}) = \widetilde{c}(1 - \widetilde{c})(\mathbf{u}_b - \mathbf{u}_u), \tag{4}$$

where subscripts b and u denote conditional ensemble averaging of $\mathbf{u}$ to burnt and unburnt regions of the field, respectively. In this context the mean is intended as the ensemble average over N images; hence, given a velocity field of the kind of $\mathbf{u}_{b,u}(x, y, t)$, its ensemble average reads $\mathbf{u}_{b,u}(x, y)$. All the results can be easily interpreted in a RANS sense. The occurrence of DL-induced effects, which are still present at $Re = 10\,000$, is confirmed by our experimental data as displayed in Fig. 13, where the turbulent flux of the averaged and filtered progress variable normal to the mean flame front is reported. In fact, for each Reynolds number shown, the DL-unstable flames are systematically characterized by a higher, positive turbulent flux, indicating an enhanced counter-gradient-type turbulent diffusion. This enhancement is only partially mitigated by the increasing Re and can be directly ascribed to the self-wrinkling of DL-unstable flames, which induce additional fluctuations acting in conjunction with standard wrinkling due to turbulence. Note that the two sets of flames whose turbulent fluxes are reported in Fig. 13 have the same equivalence ratio, thus the same expansion ratio σ. The onset of cusp-like structures in DL-unstable flames also promotes the channelling effect through the cusps, which ultimately increases the burnt conditioned velocity.

D. Transit time and crossing lengths

The flame front fluctuations and their impact on the mean reaction rate of the flame can also be effectively investigated by means of the flame transit time and crossing lengths. These concepts

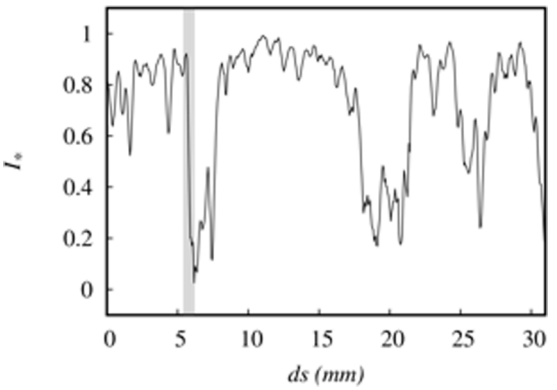

FIG. 14. Mie-scattered light intensity as measured along portion of the mean isoline $\overline{c} = 0.5$ in the 9 mm Bunsen flame at $Re = 10\,000$. Values are purposely normalized between 0 (reactants) and 1 (products), $I_* = (I - I_{\min})/(I_{\max} - I_{\min})$, with I being the scattered-light intensity. The gray rectangle represents the laminar unstrained flame front thermal thickness, which is on the order of 1 mm.

although conceived for modeling purposes in the context of RANS approaches [61], are used in this section to further characterize the structural differences between the hydrodynamically unstable and stable regimes. In fact, they can be used to assess the presence or lack thereof of a unified burning regime at higher levels of turbulence as well as consistently comparing the flame wrinkling induced by the DL instability with the one induced by turbulence. As already shown by strain-curvature j.p.d.f. and curvature correlation coefficient, a high Reynolds number common unified and turbulence dominated regime seems to be indicated, although still not completely reached.

The main features of the analytical description of mean reaction rate in turbulent flames derived in Refs. [62–64] are here briefly recalled. In the limit of high Reynolds numbers, the probability at a fixed point $\mathbf{x}$ of finding pure reactants or fully burnt mixture is described by a bimodal probability distribution function of a reaction progress variable c, defined as

$$c(\mathbf{x}, t) = \frac{T(\mathbf{x}, t) - T_r}{T_p - T_r}, \tag{5}$$

assuming $c = 0$ when the temperature equals that of the unburnt reactants $T = T_r$ and $c = 1$ in the product zone with $T = T_p$. Reactants and products are assumed separated by the flame front in the form of a thin interface keeping unaltered its laminar characteristics, commonly denoted as the *flamelet regime*. To establish the validity of flamelet hypothesis for the flames analyzed in this work, the thickness of the flame front is quantified by inspecting the velocity transition from reactants to products. To this purpose, Fig. 14 reports the light intensity scattered by 3 μm alumina particles seeding the reacting mixture in the 9 mm Bunsen flame at Reynolds number $Re = 10\,000$ [65]. This flame with its highest Karlovitz number (among those studied in this work, see the Borghi-Peters diagram of Fig. 1 for reference), is the most critical one in terms of validity of flamelet hypothesis. The scattered-light intensity is thus rapidly fluctuating between high and low values representing burnt and unburnt regions, respectively. The transition from those extreme values results to be within the thermal thickness (reported with a gray strip in Fig. 14) of the corresponding unstrained laminar flame evaluated numerically at the same conditions [53], i.e., $\Phi = 1.4$. It is thus concluded that turbulence does not alter the internal structure of the laminar flame: the flamelet hypothesis can be safely applied along with the bimodal distribution between products of combustion and reactants and the probability to find intermediates of combustion is reasonably low [66]. Note that, with our experimental data, we can access to the mean progress variable only and its instantaneous distribution is prevented. In fact, the flame front position is determined from the sudden variation of the particle number density caused by the reacting layer in premixed flames. Therefore, a nearly

bimodal intensity distribution is expected, clearly distinguishing unburnt from burnt density and the spatial average of any single binarized image results in the distribution of the mean progress variable $\overline{c}(\mathbf{x})$.

Since combustion occurs only within flamelets, the time-averaged reaction rate $\overline{\dot{\omega}}(\mathbf{x})$ at a fixed space location can be thought of as being proportional to the mean frequency $\nu(\mathbf{x})$ with which the flame front crosses the point [62,64]

$$\overline{\dot{\omega}}(\mathbf{x}) = \omega_f(\mathbf{x})\overline{\nu}(\mathbf{x}), \tag{6}$$

where ω_f represents the mean creation of products per crossing. According to the bimodal distribution hypothesis, the time signal at the point $\mathbf{x}$ can be described by a random telegraph signal of $c(\mathbf{x}, t)$ with binary values 0, 1 attained at every passage of the flame front and during the time spent in reactants $t_r(\mathbf{x}, t)$ or in products $t_p(\mathbf{x}, t)$. The mean passage times $\overline{t}_p$ and $\overline{t}_r$ are thus related to the mean progress variable $\overline{c}$ and the mean frequency ν,

$$\overline{c}(\mathbf{x}) = \frac{\overline{t}_p(\mathbf{x})}{\overline{t}_p(\mathbf{x}) + \overline{t}_r(\mathbf{x})}, \quad \nu(\mathbf{x}) = \frac{2}{\overline{t}_p(\mathbf{x}) + \overline{t}_r(\mathbf{x})}. \tag{7}$$

We can now consider the probability of finding unit value of the telegraph signal $c(\mathbf{x}, t)$ at two different instants separated by τ, in terms of covariance of c:

$$P_{11}(\mathbf{x}, \tau) = \overline{c(\mathbf{x}, t)c(\mathbf{x}, t + \tau)}. \tag{8}$$

Given the binary value 0 or 1 of the telegraph signal, $P_{11}(\mathbf{x}, \tau)$ attains notable values at extremes of τ, i.e., $\tau = 0$ and $\tau \to \infty$,

$$P_{11}(\mathbf{x}, 0) = \overline{c^2(\mathbf{x}, t)} \approx \overline{c}(\mathbf{x}), \quad P_{11}(\mathbf{x}, \tau \to \infty) = \overline{c}^2(\mathbf{x}). \tag{9}$$

This allows us to define a proper normalization of P_{11} to obtain the autocorrelation time $\hat{T}(\mathbf{x})$:

$$\hat{T}(\mathbf{x}) = \frac{1}{\overline{c}(1 - \overline{c})} \int_0^\infty (P_{11} - \overline{c}^2) d\tau. \tag{10}$$

In addition, another property for telegraph signals of the kind of $c(\mathbf{x}, t)$ leads to [67]

$$\frac{\partial P_{11}}{\partial \tau}(\mathbf{x}, 0) = -\frac{1}{2}\nu(\mathbf{x}). \tag{11}$$

To obtain an analytical expression for Eq. (10), given by the combination of Eqs. (7)–(11), it is necessary to introduce operative models for passage times, whose statistical description was first introduced [62] in the form of an exponential distribution,

$$p(t_{p,r}) = \overline{t}_{p,r}^{-1} \exp\big(-\overline{t}_{p,r}^{-1} t\big), \tag{12}$$

where the space dependence on $\mathbf{x}$ is implicitly contained in the mean passage times. This distribution was later refined in Ref. [64] to account for its unsatisfactory behavior at the shortest passage times, where the exponential distribution shows its largest occurrence, in lieu of a value tending to zero. The function proposed was the gamma-two distribution, expressed as follows:

$$p(t_{p,r}) = 4\overline{t}_{p,r}^{-2} t \exp\big(-2\overline{t}_{p,r}^{-1} t\big). \tag{13}$$

Both distributions lead to a relationship between the mean passage time ν and the integral timescale $\hat{T}$ of the autocorrelation function of the telegraph signal c, whose essential derivation from Eqs. (8) and (10) is found [62,64] to be

$$\hat{T}(\mathbf{x}) = g\frac{\overline{c}(1 - \overline{c})}{\nu(\mathbf{x})}, \tag{14}$$

with the constant g attaining the value 2 when an exponential distribution is used for the statistical description of passage times as in Eq. (12), and $g = 1$ with the gamma-two model of Eq. (13). When

Eq. (14) is substituted into Eq. (6), it leads to

$$\overline{\dot{\omega}}(\mathbf{x}) = \omega_f(\mathbf{x}) g \frac{\overline{c}(1-\overline{c})}{\hat{T}(\mathbf{x})}. \tag{15}$$

It is also shown [62] that the characteristic time $\hat{T}$ is independent of location within the flame brush.

The theoretical and modeling framework summarized above is grounded on statistics of the kind of one-point two-times. However, in the context of the measurements analyzed in this work, the most suitable statistical description is that based on one-time two-points, since ensembles of flame images are recorded. As a result, instead of a time lag τ between two instants probing the same point $\mathbf{x}$ in space, as in Eq. (8), a space lag Δ probing two different points at the same instant is employed [63]. The random telegraph signal can be defined in space rather than in time by noting that the instantaneous front shown in the images portrayed in Fig. 8 crosses the mean flame front several times, thus defining a 0, 1 binary function $c(s)$ along the curvilinear abscissa s of the mean flame front at $\overline{c} = \overline{c}^*$. Then Eq. (6) can be written for the mean reaction rate using spatial variables,

$$\overline{\dot{\omega}}(\overline{c}^*) = \omega_y(\overline{c}^*) \nu_y(\overline{c}^*), \tag{16}$$

where $\nu_y(\overline{c}^*)$ is the mean number of flame crossings from reactants to products (or vice versa) per unit distance along the abscissa s at the chosen value of the mean progress variable $\overline{c}^*$, which substitutes the dependence of position $\mathbf{x}$ in Eq. (6) and where the overline now indicates space averaging. The corresponding probability distributions of passage times described by Eqs. (12) and (13) are defined in terms of crossing lengths of products and reactants, $s_{p,r}$, which are a measure of segments corresponding to the telegraph signal being below or above the mean flame and attaining therein the values 1 or 0, respectively. For an exponential distribution

$$p(s_{p,r}, \overline{c}^*) = \overline{s}_{p,r}^{-1} \exp\left(-\overline{s}_{p,r}^{-1} s\right), \tag{17}$$

while for a gamma-two distribution

$$p(s_{p,r}, \overline{c}^*) = 4\overline{s}_{p,r}^{-2} s \exp\left(-2\overline{s}_{p,r}^{-1} s\right). \tag{18}$$

The dependence of the two distributions from the value of the mean progress variable chosen is indicated with $\overline{c}^*$. At this stage it is worth noting that when a cusp-like structure typical of DL instability crosses the mean flame, $c(s) = 0$ is found, hence an eventual trace of hydrodynamic instability is expected to affect more the reactant than the product statistics being the cusp itself a protrusion of reactants. This being said, the integral length scale L_c of the telegraph square-wave reads

$$L_c(\overline{c}^*) = \frac{1}{\overline{c}(1-\overline{c})} \int_0^\infty (P_{11} - \overline{c}^2) d\Delta, \tag{19}$$

where again $P_{11}(\Delta) = \overline{c(s)c(s+\Delta)}$ is the probability of finding two points along the isocontour $s(\overline{c}^*)$ separated by a distance Δ having both $c(s) = 1$. This results, as in Eq. (14), in a relationship between the integral length scale of the square-wave L_c and the mean number of flame crossings $\nu_y(\overline{c}^*)$ per unit distance,

$$L_c(\overline{c}^*) = g' \frac{\overline{c}(1-\overline{c})}{\nu_y(\overline{c}^*)}, \tag{20}$$

where $g' = 2$ for the exponential distribution and $g' = 1$ for the gamma-two distribution. Although less employed than the experimental results for one-point two-times statistics, the one-time two-point statistic experimental analysis shows little variation within the flame brush for L_c, as discussed in previous works [63,68,69].

Operationally, the experimental data set can now be used to analyze flame crossings at an isoline corresponding at the mean position of the flame, hence $\overline{c}^* = 0.5$. For the sake of clarity, the dependence of all the quantities from the $\overline{c}^* = 0.5$ choice will be omitted in the following

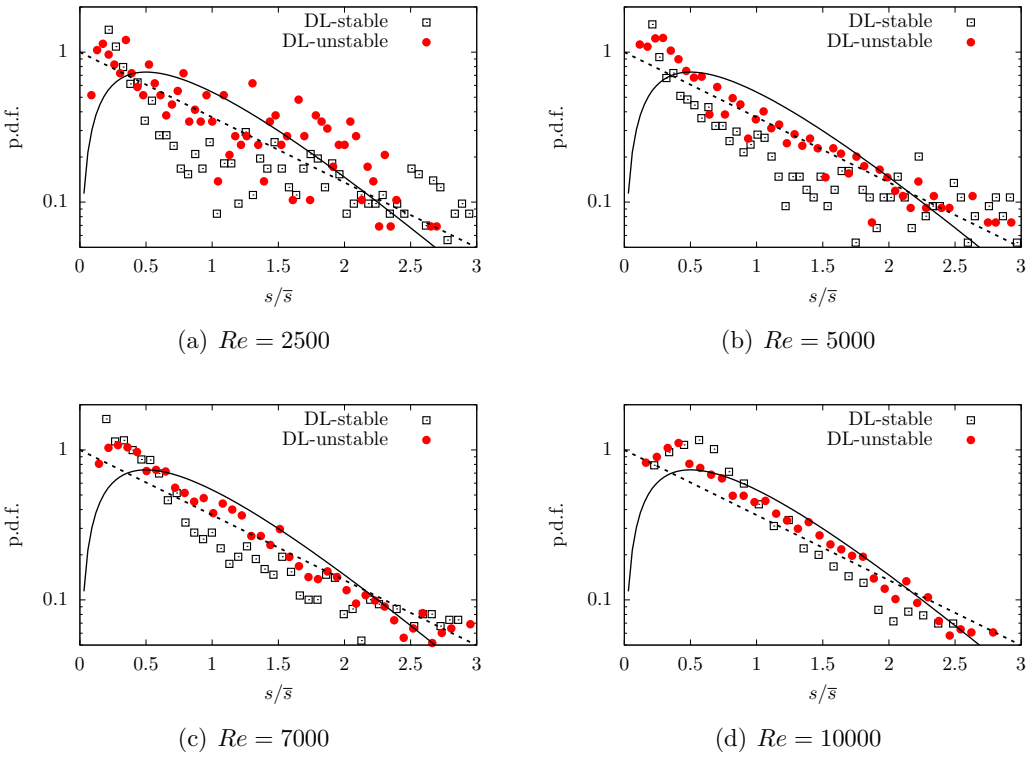

FIG. 15. P.d.f. of flame crossing lengths of reactants for DL-unstable and DL-stable flames at increasing Reynolds numbers. Values are normalized by the corresponding mean crossing length $\bar{s}$. Also reported are the reference exponential (dashed line) and gamma-two (solid line) distributions.

discussion. Instantaneous flame portions of reactants or products of combustion between two crossing points of the mean flame are defined with notation s_r and s_p, respectively. Then, with all crossing lengths measured along the mean flame contour, p.d.f.s are built for each of the recorded flame. Being cusp-like structures defined as large folds of reactants protruding into combustion products, the crossing lengths of reactants, s_r, are those mostly affected by the DL instability. The expected effect of cusp-like structures is to drag the flame front into the combustion product region reducing the extent of reactant crossing lengths with respect to product crossing lengths. In general, a cusp can be viewed as a large-scale structure comprised of a narrow central protrusion of reactants into products at high negative curvature surrounded by wider protrusions of products into reactants with a low positive curvature. This is evident from inspection of the upper panels of Fig. 8 when the instantaneous flame front crosses the mean front position $\overline{c}^* = 0.5$.

For the DL-unstable cases reported in Fig. 15, the statistics of flame crossing lengths of reactants, s_r, appear to gain, as *Re* increases, a progressively statistical behavior well fit by the gamma-two distribution, except for the low-*Re* case where no clear scaling is observed. In particular, all distributions show the maximum typical of gamma-two distribution in correspondence of values of crossing lengths comprised between 0 and 1. On the other hand, the DL-stable case, also reported in Fig. 15, shows such gamma-two distribution behavior only at the higher Reynolds number investigated, $Re = 10\,000$. This is consistent with the fact that flamelet crossing frequencies and passage time models are developed in the limit of high Reynolds numbers, as shown in several experiments [68,70], where turbulent Reynolds numbers are as large as our highest one [20,40]. In a similar fashion, the product side crossing length statistics are shown in Fig. 16 where it is still evident a lesser tendency of DL-stable flames statistics to attain clear turbulent-like shapes. In

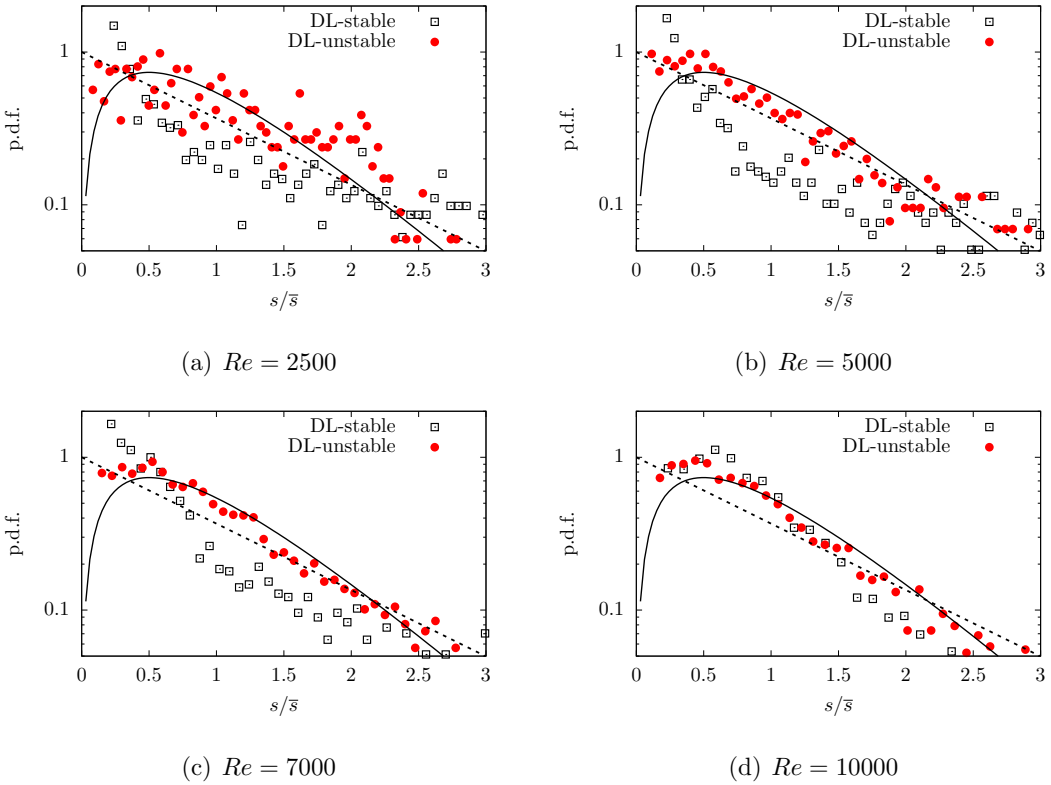

FIG. 16. P.d.f. of flame crossing lengths of products for DL-unstable and DL-stable flames at increasing Reynolds numbers. Values are normalized with the corresponding mean crossing length $\overline{s}$. Also reported are the reference exponential (dashed line) and gamma-two (solid line) distributions.

fact, also in this case, the $Re = 10\,000$ flame only follows the gamma-two distribution while other lower Reynolds number distributions scatter widely, in contrast with the DL-unstable flames whose statistics accommodate well-defined gamma-two distributions, even at lower Re.

A distinct behavior is also observed in the product and reactant crossing length differences $\overline{s}_p - \overline{s}_r$, as reported in Fig. 17. For DL-stable flames the difference is negative underlying shorter crossing length in the product side and the same difference is positive for the DL-unstable case, with longer product crossing length possibly induced by cusp-like structures shrinking the flame front, thus reducing the width of reactant length. The overall tendency is to reach a common value of zero as Reynolds number is increased, as also reported in Table III using absolute values. This is consistent with Eq. (7), which predicts $\overline{s}_r = \overline{s}_p$ at $\overline{c}^* = 0.5$.

TABLE III. Mean crossing lengths for products and reactants, $\overline{s}_p$ and $\overline{s}_r$, respectively, at different conditions.

	$D =$ 9 mm		$D =$ 18 mm	
Re	$\overline{s}_p$	$\overline{s}_r$	$\overline{s}_p$	$\overline{s}_r$
2500	8.4	9.2	12.0	11.4
5000	8.9	9.4	8.8	8.6
7000	6.8	7.5	6.7	6.9
10 000	4.3	4.4	5.7	6.1

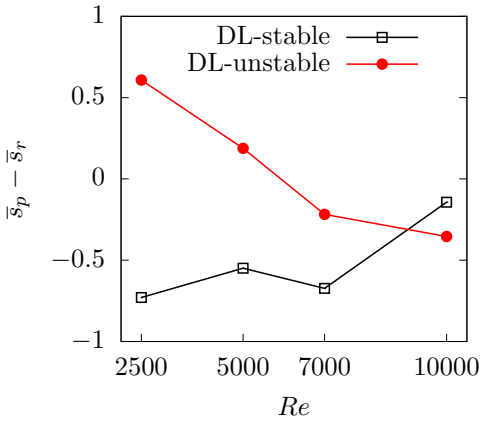

FIG. 17. Difference between product and reactant crossing lengths, $\overline{s}_p - \overline{s}_r$, as function of Re for both DL-stable and DL-unstable flames.

Figure 18(a) shows the mean number of flame crossings per unit distance along the abscissa [63] s at varying Reynolds number and for the stable and unstable cases. Results indicate a lower tendency of unstable flames to cross mean flame front per unit length, which is consistent with the observation that cusp-like structures are in the form of large scale protrusions into reactants. On the other hand, Fig. 18(c) reports, for the same conditions, the square-wave correlation lengths L_c showing that the wrinkles of DL-stable flames are constantly larger than the corresponding DL-unstable ones. In addition, as expected from the previous analysis, the differences between the DL-stable and DL-unstable cases are mitigated as Re increases. Once the mean number of crossings ν_y and the correlation length L_c have been calculated, it is possible to evaluate the constant g' appearing in Eq. (20) as reported in Fig. 18(c), recalling that $g' = 2$ represents the exponential distributions and $g' = 1$ represents the gamma-two distribution. For the DL-unstable flames, a clear statistical behavior with constant g approaching values close to 1, corresponding to a gamma-two-type distribution, is observed for all Re values with the exception of the low-Re case $Re = 2500$. On the other hand, DL-stable flames tend to establish a defined statistical behavior only at $Re = 10\,000$

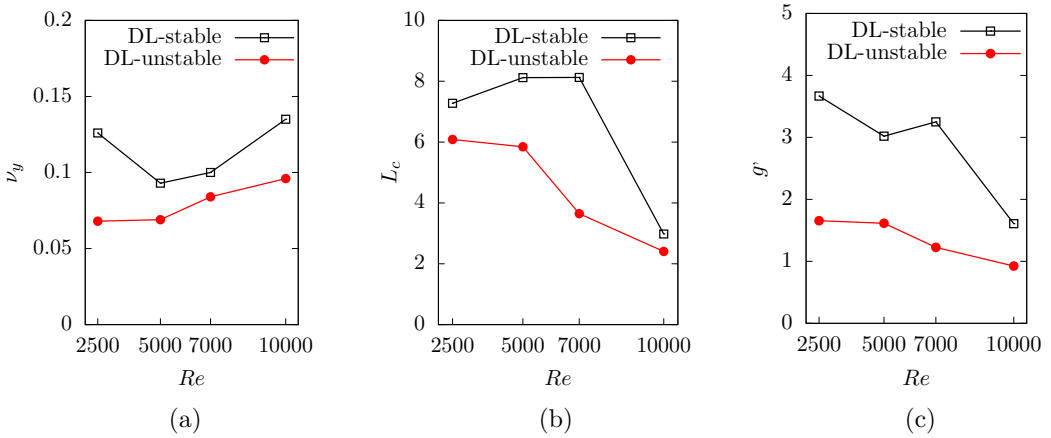

FIG. 18. Averaged values over all the available flame images as function of the Reynolds number for both the DL-unstable and DL-stable flames at the reference progress variable $\overline{c}^* = 0.5$: (a) Flame crossing per unit length ν_y. (b) Correlation length L_c. (c) Evaluation of the constant $g' = \nu_c L_c/[\overline{c}(1-\overline{c})]$.

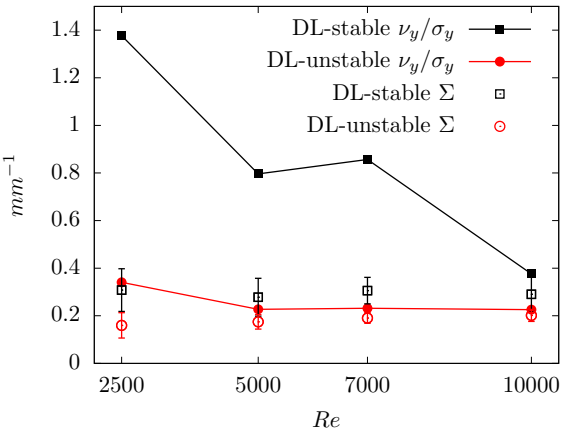

FIG. 19. Comparison of FSD evaluated as flame surface to embedding volume and $\Sigma = \nu_y/\sigma_y$ evaluated at the reference progress variable $\overline{c}^* = 0.5$.

with a g' value approaching unity. Similar results have been obtained in other works [68,69] and are corroborated by inspection of Fig. 19, which compares the flame surface density (FSD) evaluated as flame-surface to embedding-volume, calculated as discussed by Lamioni *et al.* [22], to the one derived within the BML formalism [71] as

$$\Sigma_{CL} = \frac{\nu_y(\overline{c}^*)}{\sigma_y}, \tag{21}$$

where $\nu_y(\overline{c}^*)$ is defined in Eq. (16) and σ_y is the mean magnitude of the direction cosine of angle at the intersection between the tangential direction of isoline at $\overline{c} = \overline{c}^*$ and the normal to the instantaneous flame surface. Results shows that the FSD modeled via crossing lengths and angles for DL-stable flames perform poorly at low Re, being consistent only at $Re = 10\,000$. Conversely, in DL-unstable flames, large-scale front fluctuations induced by a DL instability allow us to obtain more sound statistics.

The tools described above and the corresponding results, originally conceived for modeling purposes, have been utilized to unveil Reynolds effects on the DL instability in contrast with stable flames and quantify the differences between the two regimes. Unstable flames, even at intermediate Reynolds numbers, seem to possess the statistical characteristics that stable flames gain only with high turbulence. Results lead to conjecture that this behavior can be achieved under the influence of the self-wrinkling effect driven by hydrodynamic instability with a similar effect given by high-turbulence fluctuations. Nonetheless, the signature of DL instability emerges, as in the case of joint p.d.f. of curvature and strain of Fig. 9, where the negative correlation between curvature and strain is more pronounced than the positive one at low and intermediate Reynolds numbers and tends to equalize only at $Re = 10\,000$.

IV. CONCLUSION

In this work, we have investigated the impact of a Darrieus-Landau (DL) instability on turbulent premixed flames from low to moderate Reynolds number Re in a Bunsen configuration. We have employed well-established experimental data [20,22,40] in order to give a complete characterization of the DL-unstable Bunsen flames at low Re as well as their behavior at increasing turbulence intensity.

In a *quasilaminar*, low-Re setting, cusp-like structures have been observed in DL-unstable case ($D = 14$ mm, $\phi = 1.5$) while such features are completely absent for the DL-stable case ($D = 14$ mm, $\phi = 0.8$). The described morphological differences have been quantified in terms of

flame vorticity production and flame total strain together with its normal and tangential components. In particular, in the DL-unstable case, both the strain components are characterized by wider and less symmetric p.d.f.s when compared with their stable counterparts. Moreover, along a single DL cusp, a negative correlation between strain and curvature has been observed, which has been taken as the reference strain pattern of DL-instability for the investigation of turbulent Bunsen flames.

As *Re* is increased, the bivariate distributions between strain and curvature for the DL-unstable cases tend to deviate from the reference negative correlation given by the reference low-*Re* scatter plot. Comparing these results with the DL-stable data, some residual differences can be observed without reaching an evident completely turbulence-dominated regime. Residual differences, at increasing turbulence intensity, have also been observed for the flame curvature correlation coefficient, which is shown to be essentially independent from *Re*, consistently with an associated power spectral density analysis [40]. Moreover, such differences persist also from the modeling standpoint, as demonstrated for the turbulent flux of the averaged and filtered progress variable, where the enhanced counter-gradient-type turbulent diffusion was to be ascribed to the effect of self-wrinkling of DL-unstable flames which induces additional fluctuations acting in conjunction with standard wrinkling due to turbulence.

Since the flames investigated are expected to belong to the flamelet regime, the flame front fluctuations have been used to further characterize DL effects at increasing *Re*. Such analysis has shown that the residual morphological differences indicated by the curvature signal induce significant differences, even at higher *Re*, in terms of mean flame crossing per unit length and correlation length. This confirmation that the DL-unstable cases are characterized by lower flame surface densities in accordance with in accordance with DNS at lower *Re* [24]. It has also been found that, starting from intermediate *Re*, DL-unstable flames are characterized by *turbulent-like* statistical characteristics as a product of the DL induced self-wrinkling. The same statistical behavior, although with different values, is reached only at higher turbulence intensity by DL-stable flames. Moreover, it is found that the effects of DL instability and self-wrinkling mechanism are crucial in the BML model outcome for crossing lengths. The BML model, as expected, partially fails to describe low Reynolds stable flames, because the model is conceived for high-Reynolds-number flames only. Conversely, the BML model successfully describes low-Reynolds unstable flames. Therefore, the flame front self-wrinkling induced by the DL instability can be considered the only thing responsible for this dichotomy, making low-Reynolds unstable flames as highly wrinkled as those obtained only at high Reynolds numbers in hydrodynamically stable conditions.

The data that support the findings of this study are available upon reasonable request to the authors.

[1] C. Clanet and G. Searby, First Experimental Study of the Darrieus-Landau Instability, Phys. Rev. Lett. **80**, 3867 (1998).

[2] M. Matalon, Intrinsic flame instabilities in premixed and nonpremixed combustion, Annu. Rev. Fluid Mech. **39**, 163 (2007).

[3] M. Matalon, Flame dynamics, Proc. Combust. Inst. **32**, 57 (2009).

[4] M. Matalon, The Darrieus–Landau instability of premixed flames, Fluid Dyn. Res. **50**, 051412 (2018).

[5] E. Al Sarraf, C. Almarcha, J. Quinard, B. Radisson, and B. Denet, Quantitative analysis of flame instabilities in a Hele-Shaw burner, Flow, Turbul. Combust. **101**, 851 (2018).

[6] E. Al Sarraf, C. Almarcha, J. Quinard, B. Radisson, B. Denet, and P. Garcia-Ybarra, Darrieus–Landau instability and Markstein numbers of premixed flames in a Hele-Shaw cell, Proc. Combust. Inst. **37**, 1783 (2019).

[7] C. Altantzis, C. Frouzakis, A. Tomboulides, M. Matalon, and K. Boulouchos, Hydrodynamic and thermodiffusive instability effects on the evolution of laminar planar lean premixed hydrogen flames, J. Fluid Mech. **700**, 329 (2012).

[8] F. Creta, P. E. Lapenna, R. Lamioni, N. Fogla, and M. Matalon, Propagation of premixed flames in the presence of Darrieus–Landau and thermal diffusive instabilities, Combust. Flame **216**, 256 (2020).
[9] G. Darrieus, Propagation d'un front de flamme, La Tech. Mod. **30**, 18 (1938).
[10] L. D. Landau, On the theory of slow combustion, Acta Physicochim (URSS) **19**, 77 (1944).
[11] M. Frankel and G. Sivashinsky, The effect of viscosity on hydrodynamic stability of a plane flame front, Combust. Sci. Technol. **29**, 207 (1982).
[12] P. Clavin and F. Williams, Effects of molecular diffusion and of thermal expansion on the structure and dynamics of premixed flames in turbulent flows of large scale and low intensity, J. Fluid Mech. **116**, 251 (1982).
[13] M. Matalon and B. J. Matkowsky, Flames as gasdynamic discontinuities, J. Fluid Mech. **124**, 239 (1982).
[14] M. Matalon, C. Cui, and J. Bechtold, Hydrodynamic theory of premixed flames: Effects of stoichiometry, variable transport coefficients and arbitrary reaction orders, J. Fluid Mech. **487**, 179 (2003).
[15] B. Denet, Frankel equation for turbulent flames in the presence of a hydrodynamic instability, Phys. Rev. E **55**, 6911 (1997).
[16] F. Creta, N. Fogla, and M. Matalon, Turbulent propagation of premixed flames in the presence of darrieus–Landau instability, Combust. Theory Modell. **15**, 267 (2011).
[17] F. Creta and M. Matalon, Propagation of wrinkled turbulent flames in the context of hydrodynamic theory, J. Fluid Mech. **680**, 225 (2011).
[18] N. Fogla, F. Creta, and M. Matalon, Effect of folds and pockets on the topology and propagation of premixed turbulent flames, Combust. Flame **162**, 2758 (2015).
[19] N. Fogla, F. Creta, and M. Matalon, The turbulent flame speed for low-to-moderate turbulence intensities: Hydrodynamic theory vs. experiments, Combust. Flame **175**, 155 (2017).
[20] F. Creta, R. Lamioni, P. E. Lapenna, and G. Troiani, Interplay of darrieus-Landau instability and weak turbulence in premixed flame propagation, Phys. Rev. E **94**, 053102 (2016).
[21] R. Lamioni, P. E. Lapenna, G. Troiani, and F. Creta, Flame induced flow features in the presence of Darrieus-Landau instability, Flow, Turbul. Combust. **101**, 1137 (2018).
[22] R. Lamioni, P. E. Lapenna, G. Troiani, and F. Creta, Strain rates, flow patterns and flame surface densities in hydrodynamically unstable, weakly turbulent premixed flames, Proc. Combust. Inst. **37**, 1815 (2019).
[23] R. Lamioni, P. E. Lapenna, L. Berger, K. Kleinheinz, A. Attili, H. Pitsch, and F. Creta, Pressure-induced hydrodynamic instability in premixed methane-air slot flames, Combust. Sci. Technol. **192**, 1998 (2020).
[24] P. E. Lapenna, R. Lamioni, G. Troiani, and F. Creta, Large scale effects in weakly turbulent premixed flames, Proc. Combust. Inst. **37**, 1945 (2019).
[25] R. Yu, X.-S. Bai, and V. Bychkov, Fractal flame structure due to the hydrodynamic darrieus-Landau instability, Phys. Rev. E **92**, 063028 (2015).
[26] P. E. Lapenna, R. Lamioni, and F. Creta, Subgrid modeling of intrinsic instabilities in premixed flame propagation, Proc. Combust. Inst. **38**, 2001 (2021).
[27] A. Lipatnikov and J. Chomiak, Molecular transport effects on turbulent flame propagation and structure, Prog. Energy Combust. Sci. **31**, 1 (2005).
[28] V. Bychkov, Importance of the darrieus-Landau instability for strongly corrugated turbulent flames, Phys. Rev. E **68**, 066304 (2003).
[29] V. Akkerman and V. Bychkov, Turbulent flame and the Darrieus–Landau instability in a three-dimensional flow, Combust. Theory Modell. **7**, 767 (2003).
[30] V. Akkerman and V. Bychkov, Velocity of weakly turbulent flames of finite thickness, Combust. Theory Modell. **9**, 323 (2005).
[31] S. Chaudhuri, V. Akkerman, and C. K. Law, Spectral formulation of turbulent flame speed with consideration of hydrodynamic instability, Phys. Rev. E **84**, 026322 (2011).
[32] V. Akkerman, S. Chaudhuri, and C. K. Law, Accelerative propagation and explosion triggering by expanding turbulent premixed flames, Phys. Rev. E **87**, 023008 (2013).
[33] S. Yang, A. Saha, Z. Liu, and C. K. Law, Role of darrieus–Landau instability in propagation of expanding turbulent flames, J. Fluid Mech. **850**, 784 (2018).
[34] H. Boughanem and A. Trouvé, The domain of influence of flame instabilities in turbulent premixed combustion, Symp. (Int.) Combust. **27**, 971 (1998).

[35] S. Schlimpert, A. Feldhusen, J. Grimmen, B. Roidl, M. Meinke, and W. Schröder, Hydrodynamic instability and shear layer effects in turbulent premixed combustion, Phys. Fluids **28**, 017104 (2016).
[36] G. Troiani, F. Creta, and M. Matalon, Experimental investigation of Darrieus–Landau instability effects on turbulent premixed flames, Proc. Combust. Inst. **35**, 1451 (2015).
[37] A. Lipatnikov, W. Li, L. Jiang, and S. Shy, Does density ratio significantly affect turbulent flame speed? Flow, Turbul. Combust. **98**, 1153 (2017).
[38] X. Wang, X. Cheng, H. Lu, F. Pan, L. Qin, and Z. Wang, Effect of burner diameter on structure and instability of turbulent premixed flames, Fuel **271**, 117545 (2020).
[39] X. Wang, X. Cheng, H. Lu, Y. Xu, Y. Liu, R. Wang, and J. Yao, Quantifying the role of Darrieus–Landau instability in turbulent premixed flame speed determination at various burner sizes, Phys. Fluids **33**, 025104 (2021).
[40] P. E. Lapenna, G. Troiani, R. Lamioni, and F. Creta, Mitigation of Darrieus–Landau instability effects on turbulent premixed flames, Proc. Combust. Inst. **38**, 2885 (2021).
[41] X. Cai, J. Wang, Z. Bian, H. Zhao, Z. Li, and Z. Huang, Propagation of Darrieus–Landau unstable laminar and turbulent expanding flames, Proc. Combust. Inst. **38**, 2013 (2021).
[42] A. M. Steinberg, J. F. Driscoll, and S. L. Ceccio, Measurements of turbulent premixed flame dynamics using cinema stereoscopic PIV, Exp. Fluids **44**, 985 (2008).
[43] A. M. Steinberg and J. F. Driscoll, Straining and wrinkling processes during turbulence–premixed flame interaction measured using temporally-resolved diagnostics, Combust. Flame **156**, 2285 (2009).
[44] F. Creta and M. Matalon, Strain rate effects on the nonlinear development of hydrodynamically unstable flames, Proc. Combust. Inst. **33**, 1087 (2011).
[45] Z. Liu, V. R. Unni, S. Chaudhuri, R. Sui, C. K. Law, and A. Saha, Self-turbulization in cellularly unstable laminar flames, J. Fluid Mech. **917**, A53 (2021).
[46] A. Attili, R. Lamioni, L. Berger, K. Kleinheinz, P. E. Lapenna, H. Pitsch, and F. Creta, The effect of pressure on the hydrodynamic stability limit of premixed flames, Proc. Combust. Inst. **38**, 1973 (2021).
[47] J. Bechtold and M. Matalon, The dependence of the Markstein length on stoichiometry, Combust. Flame **127**, 1906 (2001).
[48] G. Troiani, Effect of velocity inflow conditions on the stability of a CH4/air jet-flame, Combust. Flame **156**, 539 (2009).
[49] F. Battista, F. Picano, G. Troiani, and C. M. Casciola, Intermittent features of inertial particle distributions in turbulent premixed flames, Phys. Fluids **23**, 123304 (2011).
[50] F. Picano, F. Battista, G. Troiani, and C. M. Casciola, Dynamics of PIV seeding particles in turbulent premixed flames, Exp. Fluids **50**, 75 (2011).
[51] S. Pfadler, F. Beyrau, and A. Leipertz, Flame front detection and characterization using conditioned particle image velocimetry (CPIV), Opt. Express **15**, 15444 (2007).
[52] G. Troiani and M. Marrocco, Fractal analysis of fluorescence images to assess robustness of reference-surface positioning in flame fronts, Combust. Sci. Technol. **193**, 1782 (2020).
[53] G. P. Smith, D. M. Golden, M. Frenklach, N. W. Moriarty, B. Eiteneer, M. Goldenberg, C. T. Bowman, R. K. Hanson, S. Song, W. C. Gardiner Jr., V. V. Lissianski, and Z. Qin, Gri-mech 3.0, (2017); http://www.me.berkeley.edu/gri_mech/.
[54] M. Zhang, A. Patyal, Z. Huang, and M. Matalon, Morphology of wrinkles along the surface of turbulent Bunsen flames—Their amplification and advection due to the Darrieus–Landau instability, Proc. Combust. Inst. **37**, 2335 (2019).
[55] J. F. Driscoll, Turbulent premixed combustion: Flamelet structure and its effect on turbulent burning velocities, Prog. Energy Combust. Sci. **34**, 91 (2008).
[56] S. Kheirkhah and Ö. Gülder, Turbulent premixed combustion in V-shaped flames: Characteristics of flame front, Phys. Fluids **25**, 055107 (2013).
[57] M. Boger, D. Veynante, H. Boughanem, and A. Trouvé, Direct numerical simulation analysis of flame surface density concept for large eddy simulation of turbulent premixed combustion, Symp. (Int.) Combust. **27**, 917 (1998).
[58] D. Veynante, A. Trouvé, K. Bray, and T. Mantel, Gradient and counter-gradient scalar transport in turbulent premixed flames, J. Fluid Mech. **332**, 263 (1997).

[59] G. Troiani, M. Marrocco, S. Giammartini, and C. Casciola, Counter-gradient transport in the combustion of a premixed CH4/air annular jet by combined PIV/OH-LIF, Combust. Flame **156**, 608 (2009).
[60] K. Bray and J. B. Moss, A unified statistical model of the premixed turbulent flame, Acta Astronaut. **4**, 291 (1977).
[61] T. Poinsot and D. Veynante, *Theoretical and Numerical Combustion* (RT Edwards, Inc., Philadelphia, PA, 2005).
[62] K. Bray, P. A. Libby, and J. Moss, Flamelet crossing frequencies and mean reaction rates in premixed turbulent combustion, Combust. Sci. Technol. **41**, 143 (1984).
[63] K. Bray, P. A. Libby, and J. Moss, Scalar length scale variations in premixed turbulent flames, Symp. (Int.) Combust. **20**, 421 (1985).
[64] K. Bray and P. A. Libby, Passage times and flamelet crossing frequencies in premixed turbulent combustion, Combust. Sci. Technol. **47**, 253 (1986).
[65] J. Moss, Simultaneous measurements of concentration and velocity in an open premixed turbulent flame, Combust. Sci. Technol. **22**, 119 (1980).
[66] A. Lipatnikov and J. Chomiak, Effects of premixed flames on turbulence and turbulent scalar transport, Prog. Energy Combust. Sci. **36**, 1 (2010).
[67] A. Papoulis, *Probability, Random Variables, and Stochastic Processes* (McGraw-Hill, New York, 1965).
[68] T. Chew, K. Bray, and R. Britter, Spatially resolved flamelet statistics for reaction rate modeling, Combust. Flame **80**, 65 (1990).
[69] N. Chang, S. Shy, S. Yang, and T. Yang, Spatially resolved flamelet statistics for reaction rate modeling using premixed methane-air flames in a near-homogeneous turbulence, Combust. Flame **127**, 1880 (2001).
[70] B. Deschamps, A. Boukhalfa, C. Chauveau, I. Gökalp, I. G. Shepherd, and R. K. Cheng, An experimental estimation of flame surface density and mean reaction rate in turbulent premixed flames, Symp. (Int.) Combust. **24**, 469 (1992).
[71] K. Bray, M. Champion, and P. A. Libby, The interaction between turbulence and chemistry in premixed turbulent flames, in *Turbulent Reactive Flows* (Springer, Berlin, 1989), pp. 541–563.